Materials Today Communications 26 (2021) 102022

Contents lists available at ScienceDirect

Materials Today Communications

journal homepage: www.elsevier.com/locate/mtcomm

The prediction model for additively manufacturing of NiTiHf high-temperature shape memory alloy

Mehrshad Mehrpouya [a,*], Annamaria Gisario [b], Mohammadreza Nematollahi [c], Atabak Rahimzadeh [b], Keyvan Safaei Baghbaderani [c], Mohammad Elahinia [c]

[a] Faculty of Engineering Technology, University of Twente, P.O. Box 217, 7500 AE Enschede, the Netherlands
[b] Department of Mechanical and Aerospace Engineering, Sapienza University of Rome, Via Eudossiana, 18, 00184 Rome, Italy
[c] Dynamic and Smart Systems Laboratory, Mechanical Industrial and Manufacturing Engineering Department, The University of Toledo, OH, 43606, United States

ARTICLE INFO

Keywords:
Additive manufacturing
Shape memory alloys
NiTiHf
Modeling
Artificial neural network

ABSTRACT

NiTi-based alloys are one of the most well-known alloys among shape memory alloys having a wide range of applications from biomedical to aerospace areas. Adding a third element to the binary alloys of NiTi changes the thermomechanical properties of the material remarkably. Two unique features of stability and high transformation temperature have turned NiTiHf as a suitable ternary shape memory alloys in various applications. Selective laser melting (SLM) as a layer-based fabrication method addresses the difficulties and limitations of conventional methods. Process parameters of SLM play a prominent role in the properties of the final parts so that by using the different sets of process parameters, different thermomechanical responses can be achieved. In this study, different sets of process parameters (PPs) including laser power, hatch space, and scanning speed were defined to fabricate the NiTiHf samples. Changing the PPs is a powerful tool for tailoring the thermomechanical response of the fabricated parts such as transformation temperature (TTs), density, and mechanical response. In this work, an artificial neural network (ANN) was developed to achieve a prediction tool for finding the effect of the PPs on the TTs and the size deviation of the printed parts.

1. Introduction

Shape memory effect (SME) and superelasticity (SE) result in high demand for SMAs in various engineering areas [1,2]. They are the interesting engineering behavior of SMAs that can recover the initial shape of the deformed samples in a stress-free situation or above the transformation temperature. Accordingly, they widely employ in actuation systems or damping/vibration isolation [3–5]. Among all shape memory alloys (SMAs), NiTi based alloys due to some unique properties such as high corrosion and wear resistance, large recoverable strain (8%), and biocompatibility have become of interest in many industries, biomedical, and aerospace applications [6–9]. Adding the third element to NiTi gives metallurgists a powerful tool to manipulate the SMAs properties significantly. Transformation temperature as the key factor of SMAs behavior also can be modified drastically by the presence of the third element [10,11]. Among all possible elements can be added to NiTi, Hf is of big interest to engineers due to its cost (in comparison to other elements which may increase the TTs i.e. Zr, Au, Pt, and Pd), high thermomechanical stability, as well as key features of raising the TTs of NiTi above 100 C [12–16]. NiTiHf as a high-temperature shape memory alloys (HTSMAs) has a wide range of applications in different areas such as aerospace, oil, and automotive industries [11,16,17].

Beside all these unique features making NiTi alloys, a good candidate in many industries, high tool wear, undesirable chip, and burs formation make the manufacturing of the NiTi-based alloys challenging to make the complex shape of these alloys [18–21]. This provides a significant competitive advantage for the selective laser melting (SLM) as an additive manufacturing (AM) method for metallic parts that have high flexibility [22,23] to build complex shapes layer by layer which overcomes the aforementioned manufacturing challenges [24–31]. It's well reported that the AM process parameters (PPs) such as laser power (P), scanning speed (v), hatch spacing (H), and layer thickness (t) play an important role in the thermomechanical behavior of the NiTi(Hf) fabricated parts. The correlation of these parameters can be defined in energy density ($E_V = \frac{P}{v.H.t}$) impacting the behavior of the final printed parts [25,28,29,32,33]. However, the energy density is not the only key

* Corresponding author.
E-mail address: m.mehrpouya@utwente.nl (M. Mehrpouya).

https://doi.org/10.1016/j.mtcomm.2021.102022
Received 31 December 2020; Accepted 4 January 2021
Available online 8 January 2021

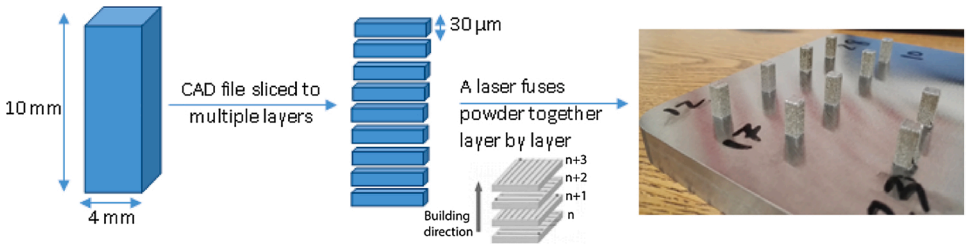

Fig. 1. A schematic of the SLM process.

factor and other PPs individually have an impact on the transformation temperatures (TTs), mechanical response, microstructure, and size of the fabricated parts [25].

Nowadays, the machine learning (ML) method has been proved a fast and reliable way to perform complex pattern recognition without solving a physical model. Among various algorithms, Artificial Neural Network (ANN) is a computational model that is widely employed for the large database to solving complicated problems using sophisticated algorithm architecture [34–36]. In reality, the ANN model is a powerful prediction tool for discovering intricate relations between input and output results, especially for nonlinear relation such as welding or AM process [37–40].

Some studies have been reported the application of the ANN method for predicting the operational parameters and consequently optimizing AM processes [41]. *Kwon et al.* applied an ANN model for the investigation on the effect of laser power in the selective laser melting (SLM) process. They performed this modeling for 13,200 melt-pool images to find out how laser power can form cracks and pores determining the quality and the density of the printed parts [42]. This approach is followed as a convolutional neural network (CNN) approach by other researchers toward robust the quality of AM parts as well as gas porosity, crack, lack of fusion, surface finish quality [43–47]. *Mehrpouya et al.* also applied the ANN models to predict the influence of the operational parameters in various laser materials processing for both metals and polymers [38,39,48]. In a particular study, they have developed a prediction model using ANN for optimizing the operational parameters in the additive manufacturing of NiTi alloy. The model showed a very good agreement between the predicted values and the experimental data with a rate of 97–99 % [49].

This paper aims to show the capabilities of the ANN model for optimizing the operational parameters in various manufacturing processes. This particular study investigates the influence of input parameters, namely laser power, laser scanning speed, and hatch spacing, in additive manufacturing of NiTiHf high-temperature shape memory alloy. In particular, the ANN model is employed as a nonlinear model to develop the correlation between inputs and the experimental results including transformation temperature (TT) and the width of the printed samples. As a result, this model can be applied as a cheap and fast prediction tool for finding the optimal operational parameters in the AM process of NiTi alloys.

2. Material and methods

The vacuum induction skull melting technique was used to produce an ingot of slightly Ni-rich Ni50.4Ti29.6Hf20 (at. %). NiTiHf powders was produced via Electrode Induction-melting Gas Atomization (EIGA) by TLS Technique GMbh (Bitterfeld, Germany). Then, the powder was sieved to achieve a size distribution of 25−75 µm. An SLM machine ProX200 Phenix Systems (currently 3D Systems) equipped with a 300 W Ytterbium fiber laser, was employed to build the parts. Printed parts had identical CAD sizes of 4*4*10 mm as shown in Fig. 1. The CAD files were then sliced into layers and multiple coupons were fabricated using different combinations of laser power (P), laser scanning speed (SS), and hatch spacing (H) which is the distance between two consecutive laser

Table 1
Process parameters of the fabricated coupons.

#	Power (w)	Hatch Space (microns)	Scan Speed (mm/s)
1	100	140	200
2	135	120	400
3	210	120	400
4	135	80	800
5	175	100	600
6	250	120	1000
7	200	60	1000
8	100	140	400
9	150	60	1000
10	150	80	200
11	250	120	200
12	210	80	400
13	250	140	466.667
14	100	60	1000
15	250	60	1000
16	250	60	733.333
17	200	140	200
18	210	120	800
19	250	140	1000
20	100	60	733.333
21	100	80	200
22	100	120	200
23	100	60	200
24	210	80	800
25	250	140	733.333
26	250	60	466.667
27	150	140	200
28	250	140	200
29	250	80	1000
30	135	80	400

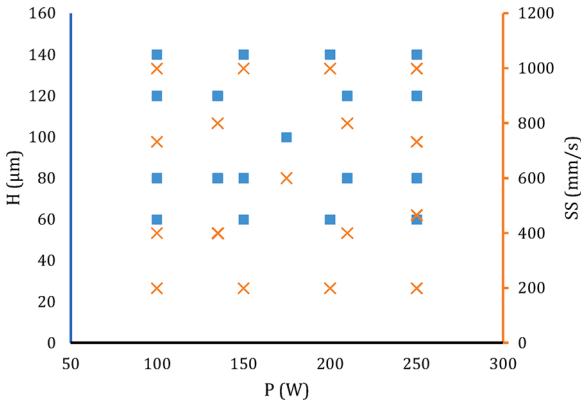

Fig. 2. Design of experiments data points. Ranges of P, SS, and H were changed systematically to see the effect of each parameter on the properties of the final part. Square and cross shapes show hatch spacing and scanning speed versus laser power, respectively.

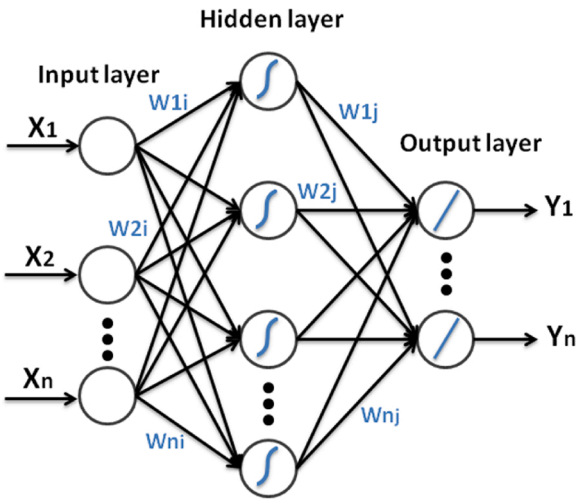

Fig. 3. A schematic of the MLP model.

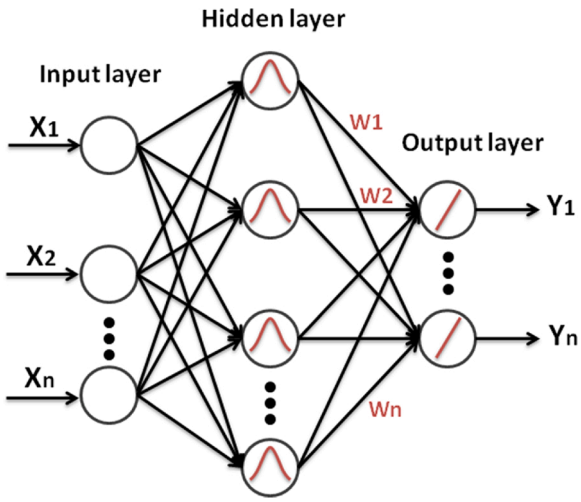

Fig. 4. A schematic of the RBF model.

passes. Since there was no available literature on process optimization of NiTiHf alloys an experiment was designed to cover wide a variety of PPs while keeping the number of samples at a reasonable number due to cost issues and difficulties in characterization. Therefore, based on our previous experience with NiTi processing optimization [49,50], P, SS, and H were changed in the range of 100−250 W, 200−1000 mm/sec, and 60−140 μm, respectively. PPs have been presented in Table 1 and schematically are shown in Fig. 2. As it is evident from Fig. 2, PPs were chosen in a way to see the effect of one parameter while the rest is constant. The layer thickness (d) was constant at 30 μm for all the conditions. We note that PPs resulted in an energy density (E = P/(SS*H*d)) range of 55.5–347.2 J/mm^3 to in one hand ensure effective melting of the powder bed to avoid porosity and on the other hand avoiding excessive temperature gradients, residual stresses, and oxidation. Argon was continuously purged inside the fabrication chamber during processing. The argon atmosphere resulted in a low oxygen level of 700 ppm and below for minimizing the impurity pick-up during the process. A bidirectional raster scanning strategy was chosen to fully meltdown the powder and create coupons as depicted in Fig. 1. Based on the ASTM standard, the TTs were determined by the tangent method from the DSC curve obtained from a Perkin-Elmer Pyris 1 Differential Scanning Calorimetry (DSC) at the heating/cooling rate of 10 C/min in the nitrogen atmosphere. DSC was run twice for each condition and Af is reported from the second trial. For the size measurements, the top, middle, and bottom parts of the coupon were measured several times and the average of the measured values is reported. More information on the fabrication process can be found in [25].

3. Neural network solution

3.1. The applied ANN models

ANN model can process a large number of information or signals in sort of simple elements to find a direct link between input and output data sets. It is inspired by biological nervous systems as well as the human brain. In general, ANN involves two phases including the phase of learning and also recall. The input and output data sets are connected with the application of the special weight rates during the learning phase, then the recall phase employs one pass using the calculated weight obtained in the learning phase. As a matter of fact, ANN can be considered as a system or model which uses many neurons to generate one or multi-layers between input and output for solving the problem [51,52]. To find the optimal operational parameters in additive manufacturing of NiTiHf alloy, this study applied two diverse ANN models, namely;

- Multi-layer perceptrons (MLP) neural network
- Radial basis function (RBF) neural network

For training the MLP neural network, specific algorithms were employed which mentioned below;

- *Levenberg–Marquardt (LM) algorithm* and an adaptive learning rate backpropagation (BP) algorithm.

The applied software in this study was used to train the neural network models using MATLAB version 2017.

3.1.1. Multi-Layer Perceptrons (MLP)

MLP is the most common type of neural network approach in use today. It has the capability to be applied for a general class of functions such as integral and continuous functions. In MLP, a group of neurons is integrated into some layers, and the first and last layers are input and output data respectively. The rest of the layers between them are hidden layers. As mentioned before, each layer receives a specific weight and transfer it to the next one. Fig. 3 illustrates a schematic of the MLP model with specified layers. The applicable formulations for the MLP model are mentioned as follows. Eq. (1) estimates the sum of all weighted input signals, then transmits to the nonlinear activation functions in Eq. (2). In the end, the network error is estimated through Eq. (3) based on a comparison between the modeling and the actual results. This process continues until to obtain an acceptable error for the process.

$$Y_{net} = \sum_{i=1}^{n} X_i . W_i + W_0 \tag{1}$$

$$Y = f(Y_{net}) = \frac{1}{1 + e^{-Ynet}} \tag{2}$$

$$J_r = \frac{1}{2} \sum_{i=1}^{k} (Y_i - O_i)^2 \tag{3}$$

Where Y_i is the response of the neuron i, $f(Y_{net})$ is the nonlinear activation function, Y_{net} is the summation of weighted inputs, X_i is the neuron input, W_i is the weight coefficient of each neuron input, W_0 is bias, J_r is the error between the observed value and network response, O_i is the observed value of the neuron i. Also, the sigmoid activation function is used in the training and testing of models in this study [53].

3.1.2. Radial Basis Function (RBF)

RBF is a class of neural networks with a wide application for solving

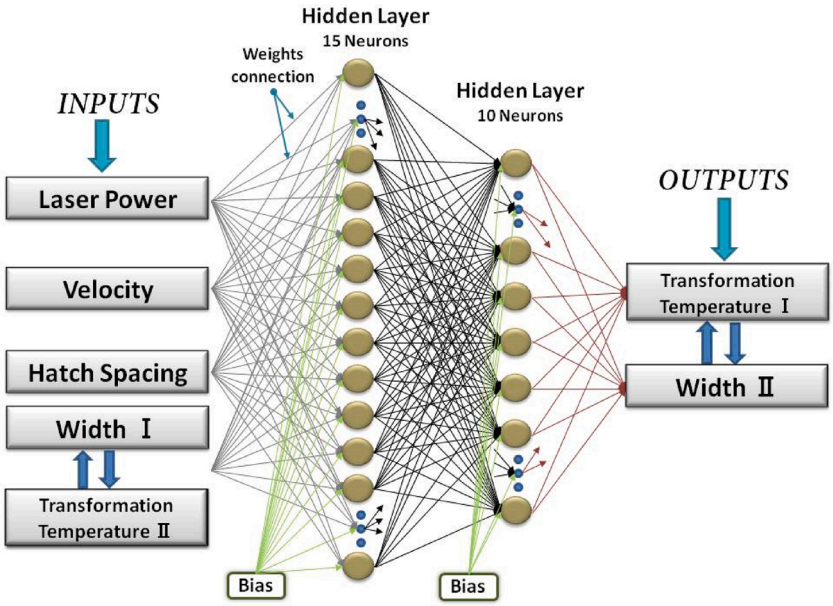

Fig. 5. A schematic of the applied neural network model.

various problems in science and engineering [54]. Similar to the MLP model, this network has three layers including input, output, and hidden layers, and the hidden layer includes a nonlinear activation function based on the multivariate Gaussian function (4), which is mentioned in below:

$$\varphi(r) = e^{\left(-\frac{1}{2\sigma_j^2}\|x-t_j\|^2\right)} \quad (4)$$

Where x is the input vector for the neuron, tj is the set of reference values, σj is the standard deviation (σ^2 is the variance) of the function for each of the centers (j), and the value r (||x-tj||) is the Euclidean distance between a center vector and the set of data points [55].

Fig. 4 depicts a schematic of the RBF model that input (X_1, X_n) and output (Y_1, Y_n) vectors are connected through radial basis functions. As can be seen, there is not a weighted between inputs and hidden layers in the RBF model while the link between the hidden layer and output is weighted [56,57]. The neurons in the hidden layer apply the functions to estimate various parameters as the final output resulting from the network.

3.2. Neural network setup

Two types of neural networks, including MLP and RBF models, were used to predicts the operational parameters in additive manufacturing of NiTiHf shape memory alloy. In particular, the experimental parameters, namely laser power, laser speed, and hatching space, were considered as the input parameters for the ANN models, while the transformation temperature and width of samples were chosen as the output of the models. All investigated samples in this modeling are divided into three groups;

- 60 % training
- 20 % cross-validation
- 20 % testing

Fig. 5 demonstrates the ANN model in this study including two hidden layers applied for both MPL and RBF models. This model includes the process parameters (laser power, laser velocity, and hatch spacing) as the inputs and also transformation temperature and sample width in the outputs. However, it is notable that the transformation temperature and sample width attend to the input subset separately to enhance the accuracy of the neural model [49,58].

Table 2
Energy density, actual size, and austenite finish temperatures of the samples.

#	Energy Input (J/mm^3)	Width (mm)	Austenite Finish Temperature (℃)	#	Energy Input (J/mm^3)	Width (mm)	Austenite Finish Temperature (℃)
1	119.0	4.72	154	16	189.4	4.5	331
2	93.8	4.58	256	17	238.1	4.74	348
3	145.8	4.6	332	18	72.9	4.34	258
4	70.3	4.33	143	19	59.5	4.09	255
5	97.2	4.61	260	20	75.8	4.38	146
6	69.4	4.08	254	21	208.3	4.8	144
7	111.1	4.28	276	22	138.9	4.78	150
8	59.5	4.42	160	23	277.8	4.8	280
9	83.3	4.26	187	24	109.4	4.41	294
10	312.5	4.92	353	25	81.2	4.36	288
11	347.2	5.05	378	26	297.6	4.66	363
12	218.8	4.72	347	27	178.6	4.78	332
13	127.6	4.51	327	28	297.6	5.05	346
14	55.6	4.09	119	29	104.2	4.25	294
15	138.9	4.25	304	30	140.6	4.58	239

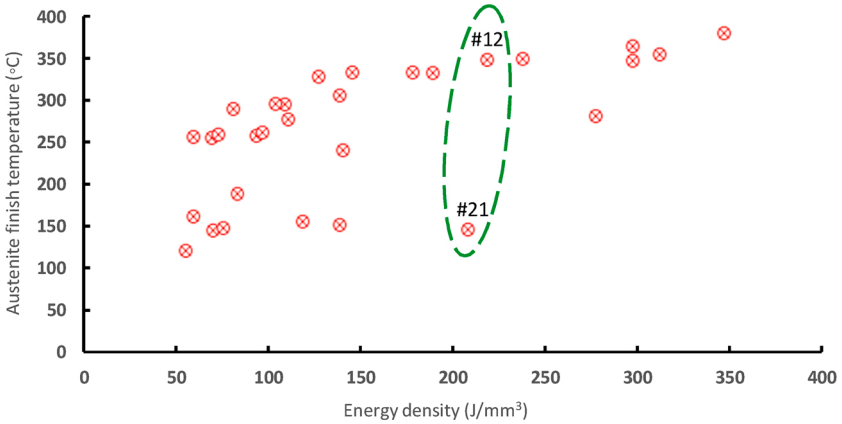

Fig. 6. The effect of energy density on the austenite finish temperature.

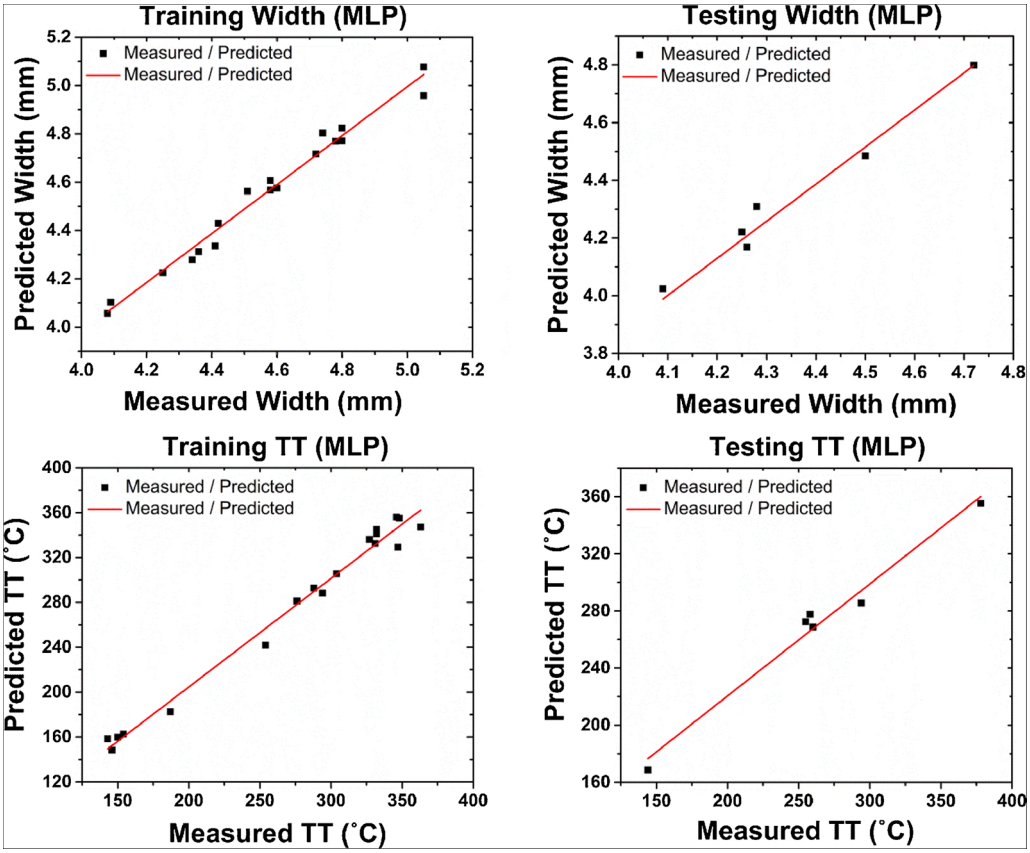

Fig. 7. Comparison between the measured and predicted width (above) and transformation temperature (bottom) in the training/testing phase for the MLP model.

4. Results and discussion

4.1. The experimental results

To evaluate the effect of PPs on the dimensional accuracy and TTs of the fabricated samples, width and austenite finish temperatures were measured and tabulated in Table 2. A size deviation up to 25 % was observed based on the condition. Energy density and scanning speed were the significant factors among PPs affecting the size of the parts. As the energy density increased, melt pools expanded and got larger, more powder was attached to the surrounding of the parts and as a result, printed samples' width varied compared to the CAD file and increased in sizes. Moreover, this size deviation was linearly increased by decreasing the scanning speed. No significant changes were observed by changing hatch spacing and laser power. In term of TTs, samples could be categorized into three different ranges (100 ℃ -200 ℃ ; 200 ℃ -300 ℃ ; 300 ℃ - 400 ℃) based on their austenite finish temperatures. There are several mechanisms affecting TTs in NiTi alloys; two of which are nickel content and impurity content (oxygen, carbon …). During the high-temperature melting process of AM, Ni evaporation is one of the main reasons that deplete the matrix resulting in higher TTs. In addition, impurities such as oxygen pick up, created Ti(Hf) precipitates which result in lower TTs. The general trend of TTs showed that the higher energy density resulted in a higher loss of Ni content from the matrix, so the TTs went up. It should be noted that the TTs were not solely affected by energy density, each individual parameter can impact the TTs. For example, based on the Austenite finish temperatures obtained from DSC curves Plotted in Fig. 6, the samples 21 ($Ev = 210\,J/mm^3$) and 12

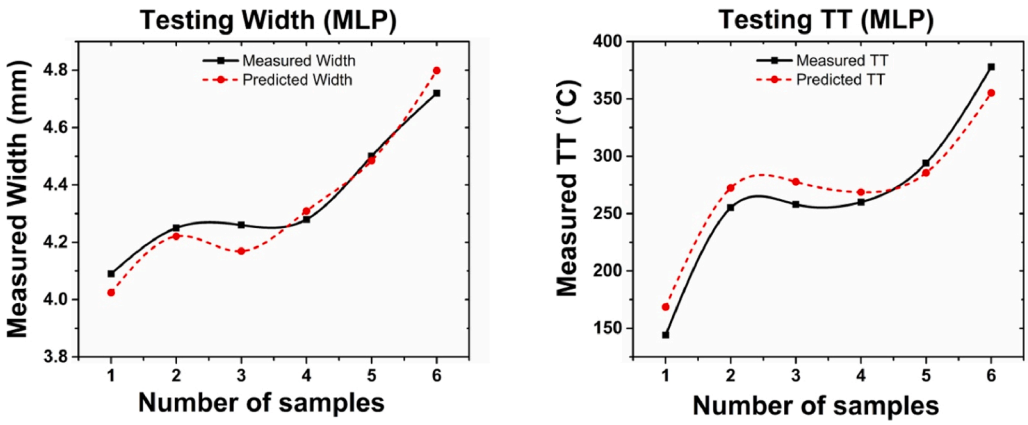

Fig. 8. The trend of testing samples for width (left) and transformation temperature (right)-MLP model.

Table 3
The statistical report of linear regression in the training/testing phase for width and transformation temperature for the MLP model.

Networks	Training	Testing
Multi-layer perceptron, MLP (Width)		
Pearson's r	0.98967	0.98797
Adj. R-Square	0.97816	0.9701
Residual sum of squares	0.02981	0.01012
Coefficient of Determination (R^2)	0.97944	0.97608
Multi-layer perceptron, MLP (TT)		
Pearson's r	0.99266	0.98936
Adj. R-Square	0.98447	0.97355
Residual sum of squares	1520.60	377.442
Coefficient of Determination (R^2)	0.98538	0.97884

(Ev = 218 J/mm^3) approximately had the same energy density, but the TTs are 144 C and 347 respectively. This showed that energy density is not the only reason for various TTs. Among PPs, laser power plays a more significant role with respect to scanning speed and hatch spacing. Based on the results, on the same level of the energy density, the higher power resulted in higher TTs. Since the focus of this paper is more on the modeling, a more in-depth analysis of the experimental data, as well as more information on the effect of PPs, can be found in [25].

4.2. Modeling of experimental data and results

The results of the ANN models, including MLP and RBF models, were compared together according to the coefficient of determination (R^2). In fact, the R^2 index represents a linear correlation between the predicted and measured values. The outcomes of the MLP model including testing

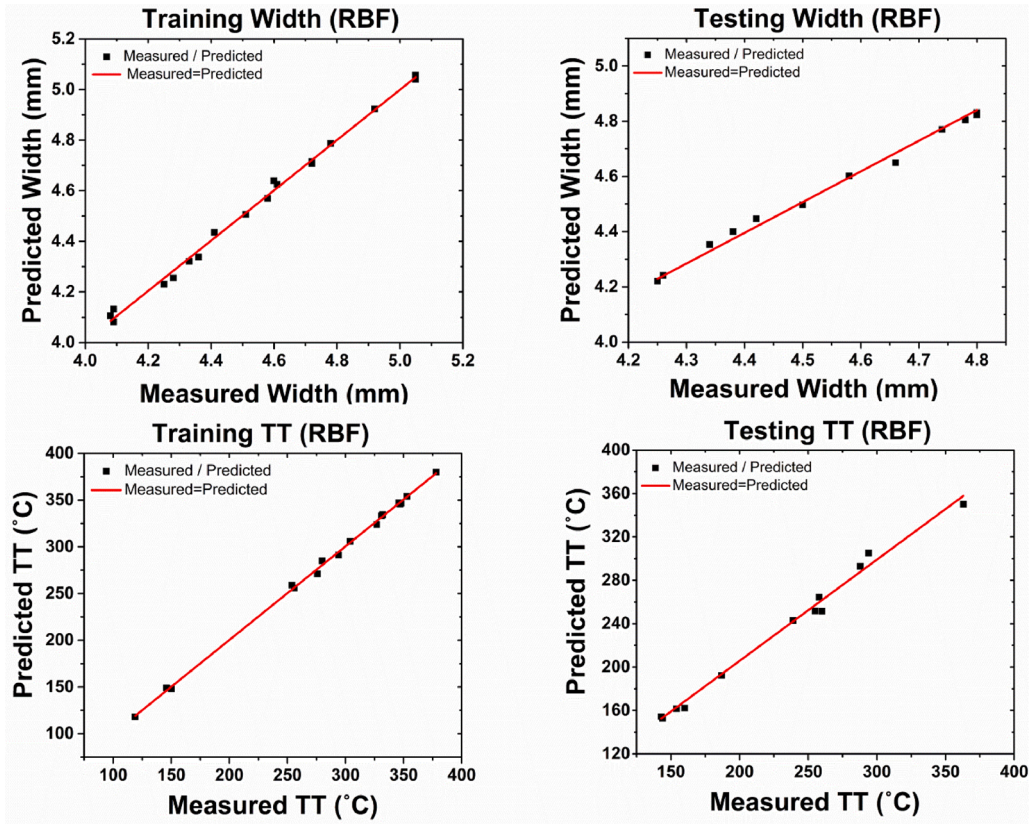

Fig. 9. Comparison between the measured and predicted width (above) and transformation temperature (bottom) in the training/testing phase for the RBF model.

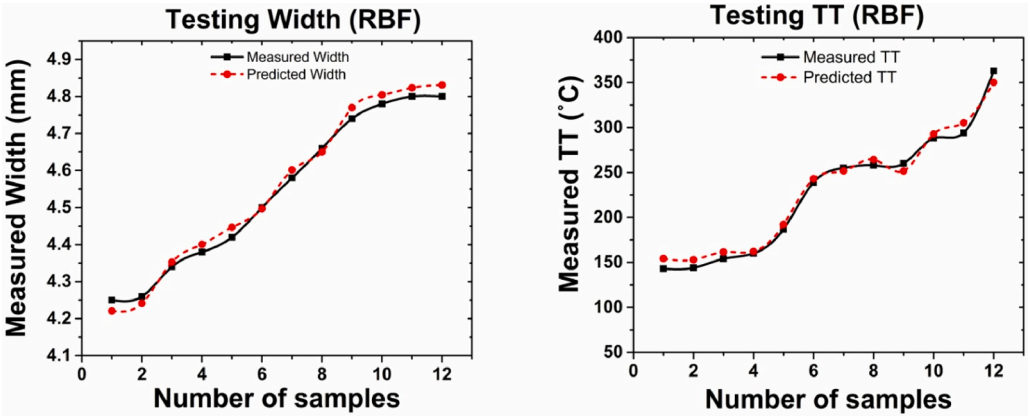

Fig. 10. The trend of testing samples for width (left) and transformation temperature (right)-RBF model.

Table 4
The statistical report of linear regression in the training/testing phase for width and transformation temperature for the RBF model.

Networks	Training	Testing
***Radial Basis Function*, RBF (Width)**		
Pearson's r	0.99792	0.99422
Adj. R-Square	0.99558	0.98731
Residual sum of squares	0.00683	0.00711
Coefficient of Determination (R^2)	0.99584	0.98846
***Radial Basis Function*, RBF (TT)**		
Pearson's r	0.99936	0.99461
Adj. R-Square	0.99864	0.98817
Residual sum of squares	129.587	520.998
Coefficient of Determination (R^2)	0.99872	0.98924

and training results for sample width (above) and transformation temperature-TT (bottom) are shown in Fig. 7. As can be seen, the graphs illustrate very good fitting lines between the measured experimental and predicted output data set.

The scatter diagram in Fig. 8 shows the trend of testing samples for both outputs, transformation temperature and width, based on the MLP model. It shows how the measured and predicted data (based on the model) are close to each other. As a result, Table 3 provides statical reports with more details regards these graphs. As visible, the R^2 index for sample width and transformation temperature are achieved by almost 97.6–97.8 %.

The results of training and testing achieved from the RBF model are shown in Fig. 9 as well. The correlation between the measured and predicted results are presented with a very good fitting for sample width (above) and transformation temperature (bottom). In the following, Fig. 10 provides the trends of testing samples for both width and TT parameters in two scatter diagrams. The predicted results from the model fit closely with the experimental results.

Table 4 provides more details related to the predicted results for the RBF model. It is notable that the amount of R^2 index is around 98.8–98.9 % for both outputs parameters including sample width and transformation temperature. This rate is only 1% higher than the MLP model, however, it statistically means a lot and shows a very good fit between the experimental data and the results achieved from the ANN model as well.

5. Conclusion

The aim of this research is to show the potential of the ANN model for achieving the optimal operational parameters in various manufacturing processes. As a matter of fact, the neural network solution can be very powerful in predicting, controlling, and managing laser processing and can be a suitable alternative to numerical and analytical models. In particular, this paper investigates two neural network models, namely MLP and RBF, to predict the operational parameters in additive manufacturing of NiTiHf alloy. Input parameters, including laser power, velocity, and hatching space, were achieved based on the experiment and utilized as the input for the neural network model as well. In this way, the performance of the models was evaluated through a comparison between the experimental data set and the regression model.

This study presented a reliable prediction model for estimating the transformation temperature and sample width based on various input parameters. The predicted parameters were evaluated quantitively using the mean error method and the coefficient of determination (R^2). The results obtained from MLP and RBF models effectively showed a good fit between the experimental and predicted data which proves the reliability of the model for predicting the printing parameters. However, the RBF neural network model represented a better agreement between the predicted values and the experimental data set with the R^2 index around 98.8–98.9 % for both transformation temperature and sample width.

CRediT authorship contribution statement

Mehrshad Mehrpouya: Conceptualization, Methodology, Writing - original draft, Supervision. **Annamaria Gisario:** Visualization, Investigation. **Mohammadreza Nematollahi:** Resources, Writing - review & editing. **Atabak Rahimzadeh:** Formal analysis, Validation. **Keyvan Safaei Baghbaderani:** Resources. **Mohammad Elahinia:** Visualization, Investigation.

Declaration of Competing Interest

The authors declare that they have no known competing financial interests or personal relationships that could have appeared to influence the work reported in this paper.

References

[1] M.H. Elahinia, Shape Memory Alloy Actuators: Design, Fabrication, and Experimental Evaluation, John Wiley & Sons, 2016.
[2] M. Mehrpouya, et al., Dissimilar laser welding of NiTi wires, Lasers Manuf. Mater. Process. 6 (2) (2019) 99–112.
[3] M. Mehrpouya, H. Cheraghi Bidsorkhi, MEMS applications of NiTi based shape memory alloys: a review, Micro Nanosyst. 8 (2) (2016) 79–91.
[4] M. Mehrpouya, A. Gisario, M. Elahinia, Laser welding of NiTi shape memory alloy: a review, J. Manuf. Process. 31 (2018) 162–186.
[5] M. Hassan, et al., Review of self-healing effect on Shape Memory Alloy (SMA) structures. Advanced Materials Research, Trans Tech Publ., 2013.
[6] M.H. Elahinia, et al., Manufacturing and processing of NiTi implants: a review, Prog. Mater. Sci. 57 (5) (2012) 911–946.
[7] N.B. Morgan, Medical shape memory alloy applications—the market and its products, Mater. Sci. Eng. A 378 (1-2) (2004) 16–23.
[8] M. Nematollahi, et al., A two-way architectural actuator using NiTi SE wire and SME spring, Int. Soc. Opt. Photon. (2018).

[9] M. Nematollahi, et al., Application of NiTi in assistive and rehabilitation devices: a review, Bioengineering 6 (2) (2019) 37.
[10] J.M. Jani, et al., A review of shape memory alloy research, applications and opportunities, Mater. Des. 56 (2014) 1078–1113.
[11] J. Ma, I. Karaman, R.D. Noebe, High temperature shape memory alloys, Int. Mater. Rev. 55 (5) (2010) 257–315.
[12] O. Benafan, et al., Viable low temperature shape memory alloys based on Ni-Ti-Hf formulations, Scr. Mater. 164 (2019) 115–120.
[13] O. Benafan, G.S. Bigelow, D.A. Scheiman, Transformation behavior in NiTi-20Hf shape memory alloys–transformation temperatures and hardness, Scr. Mater. 146 (2018) 251–254.
[14] D. Canadinc, et al., On the deformation response and cyclic stability of Ni50Ti35Hf15 high temperature shape memory alloy wires, Scr. Mater. 135 (2017) 92–96.
[15] D.R. Angst, P.E. Thoma, M.Y. Kao, The effect of hafnium content on the transformation temperatures of Ni49Ti51-xHfx. Shape memory alloys, J. Phys. Iv 5 (C8) (1995) C8–747.
[16] H.E. Karaca, et al., NiTiHf-based shape memory alloys, Mater. Sci. Technol. 30 (13) (2014) 1530–1544.
[17] O. Benafan, D.J. Gaydosh, High temperature shape memory alloy Ni50. 3Ti29. 7Hf20 torque tube actuators, Smart Mater. Struct. 26 (9) (2017), 095002.
[18] M. Elahinia, et al., Fabrication of NiTi through additive manufacturing: a review, Prog. Mater. Sci. 83 (2016) 630–663.
[19] M. Mehrpouya, et al., An investigation on the optimum machinability of NiTi based shape memory alloy, Mater. Manuf. Process. 32 (13) (2017) 1497–1504.
[20] M. Hassan, M. Mehrpouya, S. Dawood, Review of the machining difficulties of nickel-titanium based shape memory alloys. Applied Mechanics and Materials, Trans Tech Publ., 2014.
[21] M. Mehrpouya, Modeling of Machining Process of NICKEL-TITANIUM Based SHAPE MEMORY ALLOY, Department of Mechanical and Manufacturing Engineering, Faculty of …., 2013.
[22] M. Mehrpouya, et al., The potential of additive manufacturing in the smart factory industrial 4.0: a review, Appl. Sci. 9 (18) (2019) 3865.
[23] A. Gisario, et al., Metal additive manufacturing in the commercial aviation industry: a review, J. Manuf. Syst. 53 (2019) 124–149.
[24] S.E. Saghaian, et al., Mechanical and shape memory properties of triply periodic minimal surface (TPMS) NiTi structures fabricated by selective laser melting, Boil. Eng. Med 3 (2018) 1–7.
[25] M. Nematollahi, et al., Additive manufacturing of Ni-Rich NiTiHf 20: manufacturability, composition, density, and transformation behavior, Shape Mem. Superelasticity 5 (1) (2019) 113–124.
[26] M. Mahmoudi, et al., On the printability and transformation behavior of nickel-titanium shape memory alloys fabricated using laser powder-bed fusion additive manufacturing, J. Manuf. Process. 35 (2018) 672–680.
[27] M. Speirs, et al., On the transformation behavior of NiTi shape-memory alloy produced by SLM, Shape Mem. Superelasticity 2 (4) (2016) 310–316.
[28] S. Dadbakhsh, et al., Effect of SLM parameters on transformation temperatures of shape memory nickel titanium parts, Adv. Eng. Mater. 16 (9) (2014) 1140–1146.
[29] N.S. Moghaddam et al. Selective laser melting of Ni-rich NiTi: selection of process parameters and the superelastic response. International Society for Optics and Photonics.
[30] M. Elahinia, et al., Additive manufacturing of NiTiHf high temperature shape memory alloy, Scr. Mater. 145 (2018) 90–94.
[31] M. Namatollahi, et al., Additive manufacturing (AM). Metals for Biomedical Devices, 2nd edition, Woodhead Publishing, 2019, pp. 331–353.
[32] S. Saedi, et al., On the effects of selective laser melting process parameters on microstructure and thermomechanical response of Ni-rich NiTi, Acta Mater. 144 (2018) 552–560.
[33] C.A. Biffi, et al., Effect of ultrasonic nanocrystal surface modification on the microstructure and martensitic transformation of selective laser melted nitinol, Materials 12 (19) (2019) 3068.
[34] X. Qi, et al., Applying neural-network-based machine learning to additive manufacturing: current applications, challenges, and future perspectives, Engineering 5 (4) (2019) 721–729.
[35] H.P. Nagarajan, et al., Knowledge-based design of artificial neural network topology for additive manufacturing process modeling: a new approach and case study for fused deposition modeling, J. Mech. Des. 141 (2) (2019).
[36] J. Francis, L. Bian, Deep learning for distortion prediction in laser-based additive manufacturing using big data, Manuf. Lett. 20 (2019) 10–14.
[37] M.J. Somers, J.C. Casal, Using artificial neural networks to model nonlinearity: the case of the job satisfaction—job performance relationship, Organ. Res. Methods 12 (3) (2009) 403–417.
[38] M. Mehrpouya, et al., Numerical study for prediction of optimum operational parameters in laser welding of NiTi alloy, Opt. Laser Technol. 118 (2019) 159–169.
[39] M. Mehrpouya, et al., An artificial neural network model for laser transmission welding of biodegradable polyethylene terephthalate/polyethylene vinyl acetate (PET/PEVA) blends, Int. J. Adv. Manuf. Technol. (2019) 1–11.
[40] Ö. Bayraktar, et al., Experimental study on the 3D-printed plastic parts and predicting the mechanical properties using artificial neural networks, Polym. Adv. Technol. 28 (8) (2017) 1044–1051.
[41] I. Baturynska, O. Semeniuta, K. Martinsen, Optimization of process parameters for powder bed fusion additive manufacturing by combination of machine learning and finite element method: a conceptual framework, Procedia Cirp 67 (2018) 227–232.
[42] O. Kwon, et al., A deep neural network for classification of melt-pool images in metal additive manufacturing, J. Intell. Manuf. 31 (2) (2020) 375–386.
[43] W. Cui, et al., Metal additive manufacturing parts inspection using convolutional neural network, Appl. Sci. 10 (2) (2020) 545.
[44] J. Huang, et al., Surfel convolutional neural network for support detection in additive manufacturing, Int. J. Adv. Manuf. Technol. 105 (9) (2019) 3593–3604.
[45] A. Caggiano, et al., Machine learning-based image processing for on-line defect recognition in additive manufacturing, CIRP Ann. Manuf. Technol. 68 (1) (2019) 451–454.
[46] S. Chowdhury, K. Mhapsekar, S. Anand, Part build orientation optimization and neural network-based geometry compensation for additive manufacturing process, J. Manuf. Sci. Eng. 140 (3) (2018).
[47] B. Zhang, et al., Convolutional neural network-based inspection of metal additive manufacturing parts, Rapid Prototyp. J. (2019).
[48] A. Gisario, et al., Prediction model for determining the optimum operational parameters in laser forming of fiber-reinforced composites, Adv. Manuf. (2020).
[49] M. Mehrpouya, et al., A prediction model for finding the optimal laser parameters in additive manufacturing of NiTi shape memory alloy, Int. J. Adv. Manuf. Technol. 105 (11) (2019) 4691–4699.
[50] N.S. Moghaddam, et al., Achieving superelasticity in additively manufactured NiTi in compression without post-process heat treatment, Sci. Rep. 9 (1) (2019) 1–11.
[51] L. Li, S. Anand, Hatch pattern based inherent strain prediction using neural networks for powder bed fusion additive manufacturing, J. Manuf. Process. (2020).
[52] J. Jiang, et al., Analysis and prediction of printable bridge length in fused deposition modelling based on back propagation neural network, Virtual Phys. Prototyp. 14 (3) (2019) 253–266.
[53] M. Firat, M. Gungor, Generalized regression neural networks and feed forward neural networks for prediction of scour depth around bridge piers, Adv. Eng. Softw. 40 (8) (2009) 731–737.
[54] D.S. Broomhead, D. Lowe, Radial basis functions, multi-variable functional interpolation and adaptive networks. Royal Signals and Radar Establishment Malvern (United Kingdom), 1988.
[55] D.P. Aguilar, A Radial Basis Neural Network for the Analysis of Transportation Data, 2004.
[56] S. Mishra, R. Yadav, R. Singh, A survey on applications of multi layer perceptron neural networks in DOA estimation for smart antennas, Int. J. Comput. Appl. 83 (17) (2013).
[57] M. Kumar, N. Yadav, Multilayer perceptrons and radial basis function neural network methods for the solution of differential equations: a survey, Comput. Math. Appl. 62 (10) (2011) 3796–3811.
[58] M. Akbari, et al., Numerical simulation and designing artificial neural network for estimating melt pool geometry and temperature distribution in laser welding of Ti6Al4V alloy, Optik 127 (23) (2016) 11161–11172.